maize domestication and improvement. However, some of our candidate genes could be false positives, for three reasons. First, loci with very skewed frequency distributions in teosinte could lose more polymorphism during the domestication bottleneck than expected under our model, causing false inference of selection. Second, although our method confirms that the multilocus distribution of genetic diversity is inconsistent with a single bottleneck, any single gene could fall into the selected class by stochastic (nonselective) effects. Finally, rather than being the direct targets of selection, some loci could be hitchhiking with a site under selection. Indeed, candidate genes are significantly closer to the centromere than are noncandidates ($P < 0.05$), which suggests a greater chance of detecting selection in regions of reduced recombination, where hitchhiking should be more pronounced (*23*). Nonetheless, previous studies have shown that hitchhiked regions in maize tend to be relatively short (*2*, *24*), and recombination in maize coding regions is sufficient to severely limit the physical extent of hitchhiking to one, or at most a few (*25*), genes. Additionally, the subset of candidates for growth and amino acid biosynthesis are not significantly closer than noncandidate genes to the centromeres ($P = 0.49$), which suggests that these candidates are direct targets of selection.

Despite these caveats, our estimate of 2 to 4% of genes having been under selection is likely conservative, for three reasons. First, if selection acted on moderate-frequency variants in teosinte, selection may have had little effect on diversity levels (*4*). In such cases, there is little power to detect selection. Second, our method assumes that selected genes are represented by a single severe bottleneck. This approach may not detect genes subjected to subtle selection regimes. Third, high recombination rates within maize genes could reduce the hitchhiking effect to the point that only short fragments within genes retain the footprint of selection. In *tb1*, for example, selection in the promoter region did not affect diversity in the coding region (*2*). It is thus possible that we sequenced a region within a bona fide selected gene, but our region did not retain evidence of selection.

Maize domestication prompted phenotypic change that is more extensive than in most domesticated plant species. It is thus possible that maize has a higher proportion of selected genes than most domesticates, but similar studies of additional domesticated species are required to address this issue. We have shown that our candidate genes are associated with QTL regions underlying phenotypic differences between maize and teosinte, which suggests that they contribute to traits selected during domestication. Note that these genes are depauperate for polymorphism in maize, and hence it is unlikely that they could have been identified by methods that require segregating variation within maize, such as QTL or association analysis. The statistical methodology designed for this study will prove helpful both for identifying new candidates in maize and for application to other species, such as humans, where there is interest in selection on genes during the migration of modern humans out of Africa [e.g., (*26*)]. Finally, additional studies of our high-PP genes may provide important insight into the pathways and mutations responsible for maize evolution.

References and Notes

1. J. Doebley, *Annu. Rev. Genet.* **38**, 37 (2004).
2. R. L. Wang, A. Stec, J. Hey, L. Lukens, J. Doebley, *Nature* **398**, 236 (1999).
3. E. S. Buckler, J. M. Thornsberry, S. Kresovich, *Genet. Res.* **77**, 213 (2001).
4. H. Innan, Y. Kim, *Proc. Natl. Acad. Sci. U.S.A.* **101**, 10667 (2004).
5. N. Galtier, F. Depaulis, N. H. Barton, *Genetics* **155**, 981 (2000).
6. G. A. Watterson, *Theor. Popul. Biol.* **7**, 256 (1975).
7. M. I. Tenaillon, J. U'Ren, O. Tenaillon, B. S. Gaut, *Mol. Biol. Evol.* **21**, 1214 (2004).
8. L. Zhang, A. S. Peek, D. Dunams, B. S. Gaut, *Genetics* **162**, 851 (2002).
9. R. R. Hudson, *Genetics* **159**, 1805 (2001).
10. J. D. Wall, P. Andolfatto, M. Przeworski, *Genetics* **162**, 203 (2002).
11. F. Tajima, *Genetics* **123**, 597 (1989).
12. A. Eyre-Walker, R. L. Gaut, H. Hilton, D. L. Feldman, B. S. Gaut, *Proc. Natl. Acad. Sci. U.S.A.* **95**, 4441 (1998).
13. Y. Matsuoka *et al.*, *Proc. Natl. Acad. Sci. U.S.A.* **99**, 6080 (2002).
14. See supporting data on *Science* Online.
15. H. Hilton, B. S. Gaut, *Genetics* **150**, 863 (1998).
16. Y. Vigouroux *et al.*, *Mol. Biol. Evol.* **19**, 1251 (2002).
17. J. Doebley, A. Stec, C. Gustus, *Genetics* **141**, 333 (1995).
18. R. M. Clark, E. Linton, J. Messing, J. F. Doebley, *Proc. Natl. Acad. Sci. U.S.A.* **101**, 700 (2004).
19. R. Bressani, E. T. Mertz, *Cereal Chem.* **35**, 227 (1958).
20. J. Doebley, A. Stec, *Genetics* **134**, 559 (1993).
21. J. Doebley, A. Stec, *Genetics* **129**, 285 (1991).
22. J. Messing *et al.*, *Proc. Natl. Acad. Sci. U.S.A.* **101**, 14349 (2004).
23. J. Maynard Smith, J. Haigh, *Genet. Res.* **23**, 23 (1974).
24. S. R. Whitt, L. M. Wilson, M. I. Tenaillon, B. S. Gaut, E. S. t. Buckler, *Proc. Natl. Acad. Sci. U.S.A.* **99**, 12959 (2002).
25. K. Palaisa, M. Morgante, S. Tingey, A. Rafalski, *Proc. Natl. Acad. Sci. U.S.A.* **101**, 9885 (2004).
26. J. M. Akey *et al.*, *PLoS Biol.* **2**, e286 (2004).

27. We thank P. Morrell, M. Clegg, T. Long, S. McDonald, M. Przeworski, and P. Andolfatto for comments and discussion; K. Houchins, L. Schultz, and N. Duru for technical assistance; and S. Frank and L. Donaldson for use of computer clusters. Supported by NSF grants DBI0096033, DBI9872655, and DBI0321467 and by the USDA–Agricultural Research Service.

Supporting Online Material

www.sciencemag.org/cgi/content/full/308/5726/1310/DC1
Materials and Methods
Figs. S1 and S2
Tables S1 and S2
References

24 April 2005; accepted 9 May 2005
10.1126/science.1107891

Resting Microglial Cells Are Highly Dynamic Surveillants of Brain Parenchyma in Vivo

Axel Nimmerjahn,[1] Frank Kirchhoff,[2] Fritjof Helmchen[1]*

Microglial cells represent the immune system of the mammalian brain and therefore are critically involved in various injuries and diseases. Little is known about their role in the healthy brain and their immediate reaction to brain damage. By using in vivo two-photon imaging in neocortex, we found that microglial cells are highly active in their presumed resting state, continually surveying their microenvironment with extremely motile processes and protrusions. Furthermore, blood-brain barrier disruption provoked immediate and focal activation of microglia, switching their behavior from patroling to shielding of the injured site. Microglia thus are busy and vigilant housekeepers in the adult brain.

Microglial cells are the primary immune effector cells in the brain. In response to any kind of brain damage or injury, microglial cells become activated and undergo morphological as well as functional transformations. They are critically involved in lesions, neurodegenerative diseases, stroke, and brain tumors (*1*–*4*). Resident microglial cells in the healthy brain are thought to rest in a dormant state, whereas activation is associated with structural changes, such as motile branches or migration of somata (*5*, *6*). However, because most tissue preparations represent traumatic injuries by themselves, key aspects of microglia function have remained elusive.

Here, we investigated microglia behavior in intact adult brains both during the resting state and immediately after local injury by using in vivo two-photon microscopy (*7*). We used transgenic mice showing specific expression of enhanced green fluorescent protein

[1]Abteilung Zellphysiologie, Max Planck Institut für Medizinische Forschung, Jahnstrasse 29, 69120 Heidelberg, Germany. [2]Abteilung Neurogenetik, Max Planck Institut für Experimentelle Medizin, Hermann-Rein-Strasse 3, 37075 Göttingen, Germany.

*To whom correspondence should be addressed. E-mail: fritjof@mpimf-heidelberg.mpg.de

(EGFP) in resident microglia of the central nervous system (CNS). EGFP expression is achieved through placement of the EGFP reporter gene into the *Cx3cr1* locus encoding the chemokine receptor CX_3CR1 (*8*). Fluorescence images were acquired transcranially by using a thinned-skull preparation (fig. S1A) (*9*), except for cases that required direct access to the brain. Microglial cells had small rod-shaped somata from which numerous thin and highly ramified processes extended symmetrically (fig. S1B). Their three-dimensional distribution in vivo was rather homogeneous, displaying a territorial organization with typical cell-to-cell distances of 50 to 60 μm and volume densities of $6.5 \times 10^3 \pm 0.6 \times 10^3$ cells/mm^3 and $6.4 \times 10^3 \pm 0.4 \times 10^3$ cells/mm^3 in layer 1 and layer 2/3, respectively (n = 6 animals).

Time-lapse imaging experiments of up to 10 hours showed that somata of microglial cells generally remained fixed with only few signs of migration (5% of somata shifted their position by 1 to 2 μm per hour; 99 total cells; n = 12 animals). In contrast, microglial processes were remarkably motile, continuously undergoing cycles of de novo formation and withdrawal. These structural dynamics occurred on a time scale of minutes, leading to comprehensive changes in cellular morphologies within 1 hour except for a small scaffold of stable branches (Fig. 1A and movies S1 and S2). To quantify motility, we measured the velocity of length changes of individual processes. On average, extensions and retractions had similar velocities of 1.47 ± 0.10 μm/min and 1.47 ± 0.08 μm/min, respectively (Fig. 1, B and C) (range from 0.4 to 3.8 μm/min; 95 extensions and 147 retractions in 14 cells; n = 8 animals; typically, thick branches were on the lower end of this range). Branch additions and losses occurred at every branch order and balanced each other (Fig. 1D).

Microglia processes also displayed highly motile filopodia-like protrusions of variable shape, typically forming bulbous endings (Fig. 1E and movie S3). Such protrusions transiently and sometimes repeatedly appeared at various locations along the main processes and at their terminal endings. Often protrusive activity stalled for several minutes before further extension (or retraction) occurred (Fig. 1F). Time-lapse imaging at high temporal and spatial resolution revealed a high turnover of protrusions with velocities of up to 4.1 μm/min (extensions and retractions had similar rates: total average of 2.2 ± 0.2 μm/min, range from 0.6 to 4.1 μm/min, 22 extensions and 23 retractions on two cells in two animals). The average lifetime of such protrusions was 3.9 ± 0.2 min (Fig. 1, F and G) (72 protrusions in three cells; n = 3 animals; range from 1.7 to 8.3 min). Despite the constantly changing decoration of microglial processes with protrusions, the number of sites per cell showing protrusive activity remained rather constant over time (fig. S2, A and B) (mean of 19.3 ± 5.3 for n = 8 cells), as did the average total length of microglial processes (fig. S2B).

Microglial processes and protrusions sampled the extracellular space in a seemingly random fashion and at a high turnover rate. To quantify the volume fraction surveyed by microglia per time, we analyzed cumulative maximum-intensity projections through time-lapse recordings (*9*) (Fig. 2A), yielding a progressive filling rate of 14.4 ± 1.6% per hour (n = 8 animals) (Fig. 2B). Considering that the volume fraction of extracellular space is estimated to be about 20% (*10*), this suggests that the brain parenchyma is completely screened by resting microglia once every few hours. In doing so, microglial cells vary their territories. Border zones between neighboring microglial cells were mutable, and changes in favor of adjacent cells

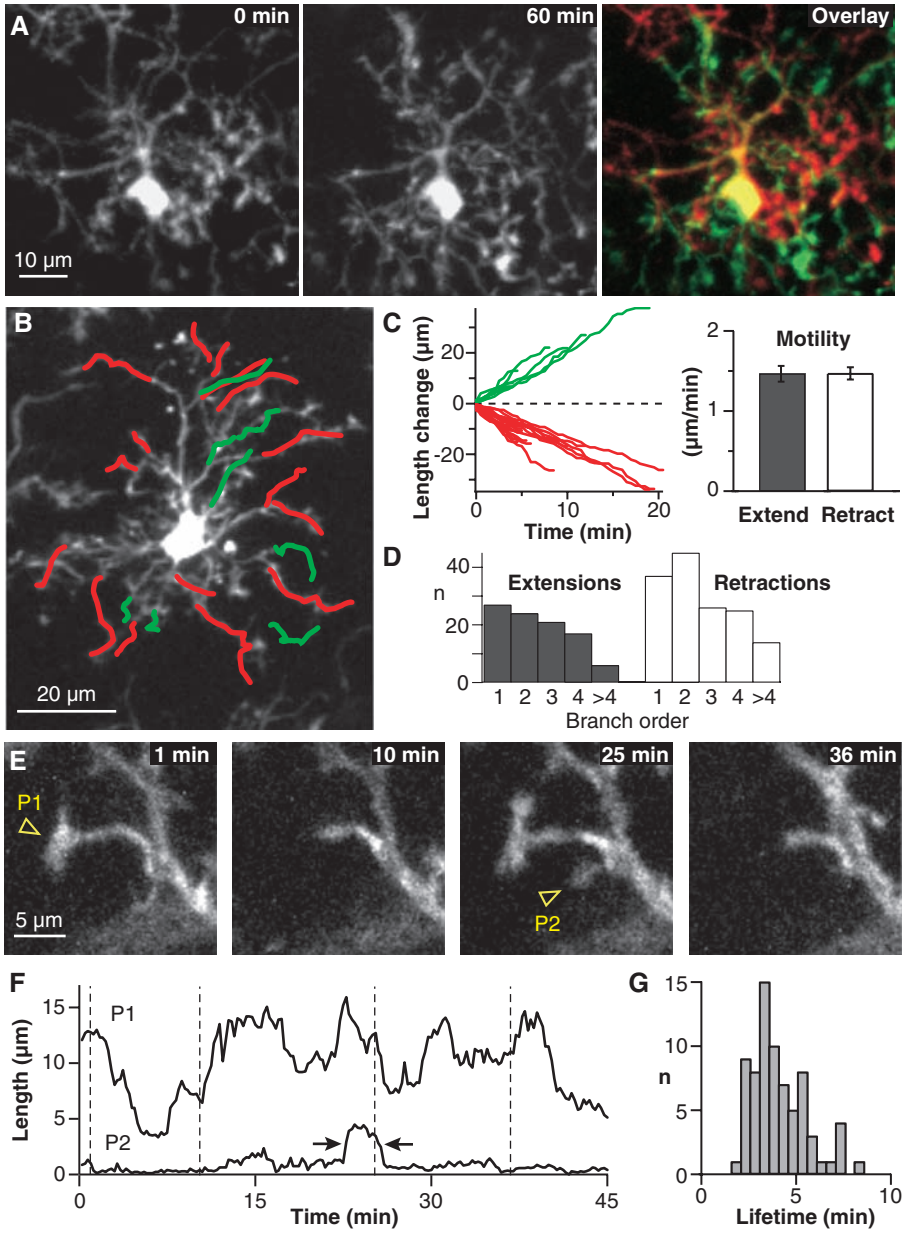

Fig. 1. Microglial cells are highly dynamic in the resting state in vivo. (**A**) Maximum-intensity projections of an individual microglial cell (45 to 75 μm below the pia) at the beginning (left) and 1 hour after (center) the start of a transcranial time-lapse recording. (Right) Overlay showing extensive formation (green) and deletion (red) of microglial processes. (**B**) Extensions (green) and retractions (red) of processes over the time course of 20 min. (**C**) Length changes of the processes shown in (B) as a function of time. (Right) Mean motility values in μm/min for extensions and retractions. (**D**) Branch motility occurred at every branch order. (**E**) Example images of microglial protrusions (arrowheads) from a time-lapse recording. (**F**) Length changes over time of the two protrusions P1 and P2 indicated in (E). Vertical dashed lines mark the acquisition times of the images shown in (E). Arrows indicate protrusion lifetime (*9*). (**G**) Lifetime histogram of protrusions.

often occurred after retraction of thick processes in another cell. When processes of neighboring microglial cells encountered one other, endings mutually repelled each other.

This high resting motility may serve a housekeeping function, enabling microglial cells to effectively control the microenvironment and to clear the parenchyma of accumulated (low diffusible) metabolic products and deteriorated tissue components. Indeed, branch protuberances of microglial cells were short-lived and typically showed bulbous endings, indicating that tissue material had been collected. In a few cases, we observed spontaneous engulfments of tissue components, which subsequently were transported toward the soma (Fig. 2C and movie S4). To further reveal the interaction between microglia and other cortical elements, we counterstained astroglia with the red fluorescent dye sulforhodamine 101 (SR101) (*11*). Control imaging experiments before, during, and after SR101 application showed no adverse effects of SR101 itself on microglia motility (n = 4 animals). Unlike microglial cells, astrocytes showed no comparable restructuring of their processes. The SR101 counterstain also enabled us to visualize neuronal cell bodies and cortical blood vessels, which appear as unstained dark areas (Fig. 2D). Microglia processes and protrusions directly contacted astrocytes, neuronal cell bodies, and blood vessels, suggesting that in the healthy brain microglia dynamically interact with other cortical elements (Fig. 2D and movie S5). Because microglia are thought to monitor neuronal well-being through molecular changes in their microenvironment (*12*), we tested whether a change in the level of neuronal activity might affect microglia behavior. Surface application of the ionotropic γ-aminobutyric acid (GABA) receptor blocker bicuculline (BCC, 50 μM) was found to significantly increase microglia volume sampling, whereas application of the sodium channel blocker tetrodotoxin (TTX, 25 to 50 μM) had no significant effect [Supporting Online Material (SOM) Text, fig. S3, and movie S6].

Another likely function of the high resting microglia motility is to facilitate prompt reactions to brain injury (*5*). We therefore characterized microglia activation immediately after targeted disruption of the blood-brain barrier (BBB) at the level of individual capillaries (Fig. 3). Vessel outlines were visualized with the use of SR101 application. After a baseline imaging period, individual capillaries of about 6 μm diameter were damaged by using highly localized laser lesions either through the thinned skull or through a small cranial window (Fig. 3A and movie S7). Disruption of the BBB was indicated by local tissue expansion and detachment of astroglial end feet. Laser lesions caused extravasation of dye in three experiments in which blood plasma was stained via tail-vein injection of a dextran-conjugated fluorescent dye (movie S8). Laser lesions induced an immediate microglia response, indicated by a switch from undirected to targeted movement of nearby microglial processes toward the injured site (Fig. 3B and movies S7 and S9). The average velocity of extensions radially impinging on the injured site was similar to extension rates during the resting state (mean of 1.8 ± 0.3 μm/min for n = 5 animals). Processes on the far side of activated microglial cells subsequently started to retract.

The number of responding microglial cells depended on the severity of the injury. In general, only microglial cells in the immediate vicinity of the microlesion were activated, whereas cells farther away (>90 μm) did not or did not immediately respond. In two cases, laser lesions caused a transient activation of only a single microglial cell. In those cases, no measurable tissue expansion was observed, indicating only mild damage to the BBB. Yet in all lesion experiments, shielding of the injured area through accumulation of microglial extensions was observed (Fig. 3B and movie S10). In cases of severe BBB disruption, multiple spherical-shaped inclusions started to form around 10 to 15 min after the lesion, indicating phagocytic activity by microglial processes. Inclusions were found within 15- to 25-μm radial distances of the injured site, showing diverse dimensions with an average diameter of 4.6 ± 0.3 μm (Fig. 3, C and D and movie S11) (range from 4.6 to 11.1 μm; n = 34 inclusions in two animals). Inclusions were stable for several minutes (mean of 11.6 ± 1.9 min and range from 1.8 to 23.9 min) before they rapidly collapsed (mean of 2.0 ± 0.5 min; n = 14 inclusions in two animals) to around 40% of their initial size (Fig. 3E). Notably, the larger the inclusions, the shorter their lifetimes. Within the observation period (up to 5.5 hours), somata of microglial cells became more rounded. They did not, however, migrate toward the injured site. Interestingly, SR101-colabeled astrocytes showed no morphological response to the laser-induced microstroke. A switch from undirected surveillance behavior to targeted

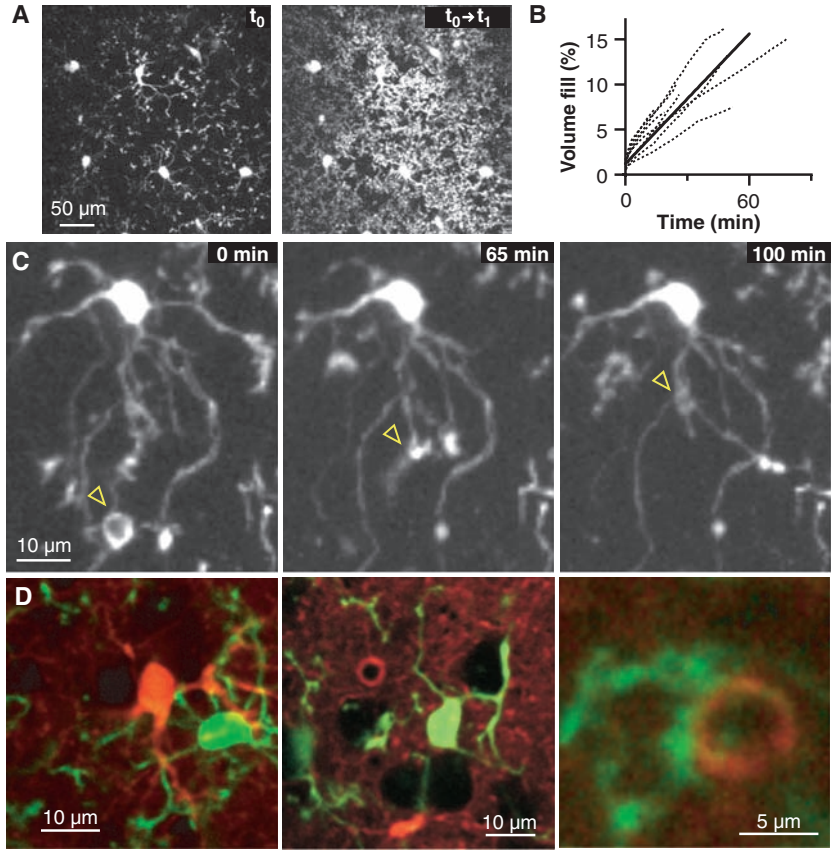

Fig. 2. Resting microglia continuously sample their microenvironment and dynamically interact with other cortical elements. (**A**) Example images illustrating cumulative volume sampling. (Left) Initial image at time t_0. (Right) Cumulative projection at a later time point, t_1 (*9*). (**B**) Quantitation of volume sampling. Dashed lines, percentage increases for individual cells; solid line, average trace. (**C**) Example images from a time-lapse recording showing spontaneous engulfment and subsequent evacuation of tissue components by microglial processes (yellow arrowheads). (**D**) Example images showing how microglial processes and protrusions contact neighboring astrocytes (left), neuronal cell bodies (center; unstained dark areas), and the astrocytic sheath around a microvessel (right). Images are overlays of the green microglia and red SR101 stain.

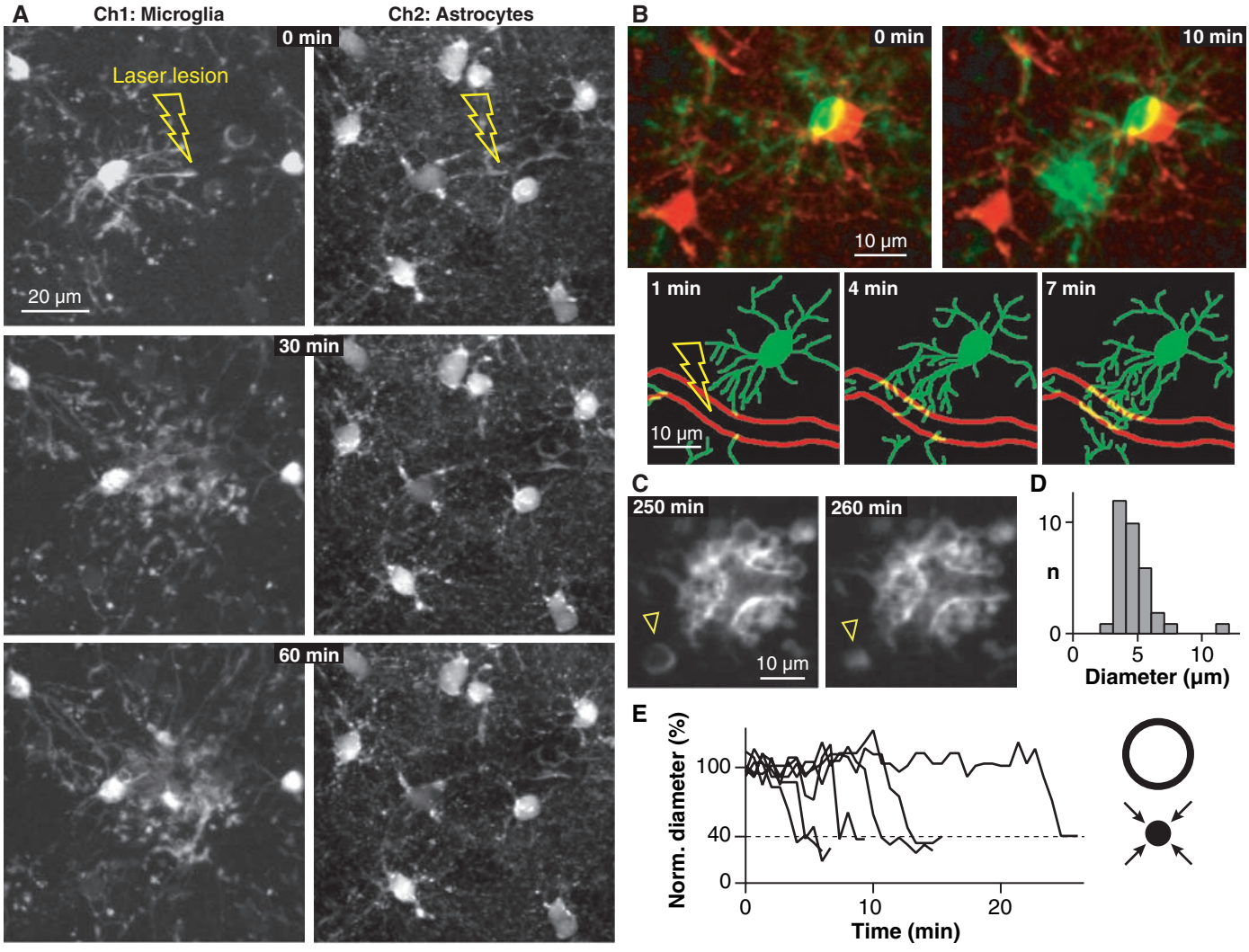

Fig. 3. Microglia are rapidly activated after local BBB disruption. (**A**) Fluorescence images of EGFP-expressing microglial cells (Ch1) and SR101 counterstained astrocytes (Ch2) before, 30 min, and 60 min after a targeted laser-induced microlesion. The disrupted blood vessel is apparent in Ch2 (yellow flashes indicate the site of injury). (**B**) Rapid shielding of a lesioned blood vessel section. (Top) Overlay of green microglia and red-stained astrocytes before and 10 min after the laser-induced lesion. (Bottom) Microglia morphology at intermediate time points showing rapid, targeted movement of microglial processes toward the injured blood vessel (outlined in red; yellow flash indicates the site of injury). (**C**) Activated microglia processes at the site of laser lesion about 4 hours after injury. Several spherical engulfments are visible in the vicinity of the lesioned blood vessel arborization. Arrowhead points to an engulfment that collapsed within a few minutes. (**D**) Histogram of the diameter distribution of 33 postlesion engulfments. (**E**) (Left) Example time courses of spherical shaped engulfments. Diameters are normalized to initial values. (Right) Schematic illustrating the collapse of an engulfment.

movement of microglial processes was also observed in response to local lipopolysaccharide application (SOM Text).

Our results demonstrate that microglial cells are highly dynamic structures during the "resting" state in vivo and not only after activation. The extent of ongoing structural changes far exceeds what has been described for both neurons (*13*, *14*) and astrocytes (*15*) on a similar time scale (SOM Text). The pronounced and ongoing structural changes of resting microglial cells presumably serve an immune surveillance function (SOM Text). In particular, microglia can sense subtle changes in their microenvironment through a variety of surface receptors, such as purino- and fractalkine receptors (*12*), receptors for complement fragments, immunoglobulins, adhesion molecules, and inflammatory stimuli (*16*). In addition, microglia can respond to these changes, for example, through expression of neurotrophic factors or release of pro- and anti-inflammatory cytokines upon activation (*12*). Our experiments suggest that microglia perform this surveillance function by continuously sampling their environment with highly motile protrusions. These protrusions may also be involved in collecting tissue debris. Microglia motility most likely has its basis in actin, a cytoskeletal protein shown to be critically involved in growth and motility in many cells. Indeed, microglia contain high amounts of filamentous actin (*17*), and inhibitors of actin polymerization have been shown to affect the motility and migration of activated microglial cells (*5*).

Activated microglia are thought to exert neuroprotective as well as neurotoxic functions on neurons. Overall this effect may depend on both pathologic conditions and injury severity (*12*, *16*). In our microlesion experiments, the shielding of injured sites indicated a neuroprotective role for microglia. Furthermore, the early formation of spherical-shaped inclusions suggests immediate phagocytic engulfment and removal of damaged tissue or leaked blood components. Together, this is consistent with the idea that microglia constitute the first line of defense against invading pathogens (*12*, *18*). In conjunction with animal models of brain disease, our in vivo imaging approach presents the opportunity to study the role of microglia in various pathologies in the intact brain.

References and Notes

1. G. W. Kreutzberg, *Trends Neurosci.* **19**, 312 (1996).
2. G. Stoll, S. Jander, *Prog. Neurobiol.* **58**, 233 (1999).
3. W. J. Streit, *Glia* **40**, 133 (2002).
4. W. J. Streit, *J. Neurosci. Res.* **77**, 1 (2004).
5. C. Nolte, T. Moller, T. Walter, H. Kettenmann, *Neuroscience* **73**, 1091 (1996).
6. N. Stence, M. Waite, M. E. Dailey, *Glia* **33**, 256 (2001).
7. W. Denk, K. Svoboda, *Neuron* **18**, 351 (1997).
8. S. Jung *et al.*, *Mol. Cell. Biol.* **20**, 4106 (2000).
9. Materials and methods are available as supporting material on *Science* Online.
10. A. Lehmenkuhler, E. Sykova, J. Svoboda, K. Zilles, C. Nicholson, *Neuroscience* **55**, 339 (1993).
11. A. Nimmerjahn, F. Kirchhoff, J. N. D. Kerr, F. Helmchen, *Nat. Methods* **1**, 31 (2004).
12. D. van Rossum, U. K. Hanisch, *Metab. Brain Dis.* **19**, 393 (2004).
13. J. Grutzendler, N. Kasthuri, W. B. Gan, *Nature* **420**, 812 (2002).
14. J. T. Trachtenberg *et al.*, *Nature* **420**, 788 (2002).
15. J. Hirrlinger, S. Hulsmann, F. Kirchhoff, *Eur. J. Neurosci.* **20**, 2235 (2004).
16. G. Raivich *et al.*, *Brain Res. Rev.* **30**, 77 (1999).
17. F. Capani, M. H. Ellisman, M. E. Martone, *Brain Res.* **923**, 1 (2001).
18. F. Vilhardt, *Int. J. Biochem. Cell Biol.* **37**, 17 (2005).

19. We thank S. Erdogan for help with the analysis, J. N. D. Kerr and G. W. Kreutzberg for comments on the manuscript, S. Jung and D. R. Littman for providing the green fluorescent microglia mouse line, and B. Sakmann for generous support. This work was supported by a predoctoral fellowship of the Boehringer Ingelheim Fonds to A.N.

Supporting Online Material
www.sciencemag.org/cgi/content/full/1110647/DC1
Materials and Methods
SOM Text
Figs. S1 to S3
References and Notes
Movies S1 to S12

3 February 2005; accepted 17 March 2005
Published online 14 April 2005;
10.1126/science.1110647
Include this information when citing this paper.

Structural Bioinformatics-Based Design of Selective, Irreversible Kinase Inhibitors

Michael S. Cohen, Chao Zhang, Kevan M. Shokat, Jack Taunton*

The active sites of 491 human protein kinase domains are highly conserved, which makes the design of selective inhibitors a formidable challenge. We used a structural bioinformatics approach to identify two selectivity filters, a threonine and a cysteine, at defined positions in the active site of p90 ribosomal protein S6 kinase (RSK). A fluoromethylketone inhibitor, designed to exploit both selectivity filters, potently and selectively inactivated RSK1 and RSK2 in mammalian cells. Kinases with only one selectivity filter were resistant to the inhibitor, yet they became sensitized after genetic introduction of the second selectivity filter. Thus, two amino acids that distinguish RSK from other protein kinases are sufficient to confer inhibitor sensitivity.

Phosphorylation of serine, threonine, and tyrosine residues is a primary mechanism for regulating protein function in eukaryotic cells. Protein kinases, the enzymes that catalyze these reactions, regulate essentially all cellular processes and have thus emerged as therapeutic targets for many human diseases (*1*). Small-molecule inhibitors of the Abelson tyrosine kinase (Abl) and the epidermal growth factor receptor (EGFR) have been developed into clinically useful anticancer drugs (*2*, *3*). Selective inhibitors can also increase our understanding of the cellular and organismal roles of protein kinases. However, nearly all kinase inhibitors target the adenosine triphosphate (ATP) binding site, which is well conserved even among distantly related kinase domains. For this reason, rational design of inhibitors that selectively target even a subset of the 491 related human kinase domains continues to be a daunting challenge.

Structural and mutagenesis studies have revealed key determinants of kinase inhibitor selectivity, including a widely exploited selectivity filter in the ATP binding site known as the "gatekeeper." A compact gatekeeper (such as threonine) allows bulky aromatic substituents, such as those found in the Src family kinase inhibitors, PP1 and PP2, to enter a deep hydrophobic pocket (*4*–*6*). In contrast, larger gatekeepers (methionine, leucine, isoleucine, or phenylalanine) restrict access to this pocket. A small gatekeeper provides only partial discrimination between kinase active sites, however, as ~20% of human kinases have a threonine at this position. Gleevec, a drug used to treat chronic myelogenous leukemia, exploits a threonine gatekeeper in the Abl kinase domain, yet it also potently inhibits the distantly related tyrosine kinase, c-KIT, as well as the platelet-derived growth factor receptor (PDGFR) (*7*).

We therefore sought a second selectivity filter that could be discerned from a primary sequence alignment. Among the 20 amino acids, cysteine has unique chemical reactivity and is commonly targeted by electrophilic inhibitors. In the case of cysteine protease inhibitors, the reactive cysteine is not a selectivity filter, because it is found in every cysteine protease and is essential for catalysis. Electrophilic, cysteine-directed inhibitors of the EGFR kinase domain have also been reported (*8*), but here again, the cysteine does not act as a selectivity filter, because neither the electrophile nor the reactive cysteine is required for potent, selective inhibition by these compounds. In this report, we describe the rational design of selective kinase inhibitors that require the simultaneous presence of a threonine gatekeeper and a reactive cysteine, which are uniquely found in the C-terminal kinase domain of p90 ribosomal protein S6 kinases (RSKs).

We used a kinomewide sequence alignment (*1*, *9*) to search for cysteines that, together with a threonine gatekeeper, could form a covalent bond with an inhibitor in the ATP pocket. We focused on the conserved glycine-rich loop, which interacts with the triphosphate of ATP and is one of the most flexible structural elements of the kinase domain (*10*). A cysteine near this solvent-exposed loop is likely to have a lower pK_a and therefore to be more reactive than a cysteine buried in the hydrophobic pocket. Out of 491 related kinase domains in the human genome (*1*), we found 11 with a cysteine at the C-terminal end of the glycine-rich loop (Fig. 1A), a position usually occupied by valine. We next examined the gatekeeper in these

Table 1. Half-maximal inhibitory concentrations (IC_{50} in μM) for fmk and the pyrrolo[2,3-*d*]pyrimidine scaffold against the kinase activities of wild-type (WT) and mutant RSK2 CTDs. RSK2 CTDs were expressed in *E. coli* as His_6-tagged proteins and activated by incubation with bacterially expressed His_6-ERK2 and ATP. Kinase assay conditions: 30-min inhibitor pretreatment, 1 nM RSK2 CTD, 0.1 mM ATP, 0.1 mM "CTD-tide" substrate (*14*). WT and mutant CTDs had similar kinase activities.

	WT	C436V	T493M
fmk	0.015 ± 0.001	>10	3.4 ± 0.3
scaffold	1.2 ± 0.08	0.43 ± 0.14	>30

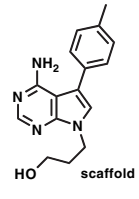

Program in Chemistry and Chemical Biology, and Department of Cellular and Molecular Pharmacology, University of California, San Francisco, CA 94143–2280, USA.

*To whom correspondence should be addressed. E-mail: taunton@cmp.ucsf.edu